

## Phosphorus and Carbon Co-Doped TiO<sub>2</sub> Nanotube Arrays for Excellent ROS Production

Srimala Sreekantan<sup>1</sup>, Khairul Arifah Saharudin<sup>1</sup>, Norfatehah Basiron<sup>1</sup>, Rabiatal Basria S. M. N. Mydin<sup>2</sup>, Ong Cheok Teng<sup>1</sup>, and Vignesh Kumaravel<sup>3</sup>

<sup>1</sup>School of Materials and Mineral Resources Engineering, Engineering Campus, Universiti Sains Malaysia, 14300 Nibong Tebal, Penang, Malaysia; <sup>2</sup>Advanced Medical and Dental Institute, Universiti Sains Malaysia, Bertam, 13000 Kepala Batas, Penang, Malaysia; <sup>3</sup>Chemical Engineering Program, Texas A & M University at Qatar, Doha-23874, Qatar

Correspondence: srimala@usm.my (S.S.), rabiatalbasria@usm.my (R.B.M.)

*Sreekantan S et al. Reactive Oxygen Species 6(17):349–362, 2018; ©2018 Cell Med Press*  
<http://dx.doi.org/10.20455/ros.2018.853>

(Received: December 26, 2017; Revised: May 21, 2018; Accepted: May 22, 2018)

**ABSTRACT** | Carbon (C) and phosphorus (P) co-doped TiO<sub>2</sub> nanotube arrays (TNA) were prepared by the anodization method. To evaluate the release of reactive oxygen species (ROS) under visible light response, the synthesized samples that was annealed at 400°C were characterized through scanning electron microscopy (SEM), X-ray diffraction (XRD), and photoluminescence spectroscopy (PL) techniques. Methylene blue (MB) was used as a target pollutant and a scavenger test was conducted to evaluate the release of ROS from TNA. TNA with different morphology attained by varying the concentration of H<sub>3</sub>PO<sub>4</sub> and ethylene glycol (EG) during anodization. TNA with 3.1 μm length and 103 nm average diameter were obtained using 90 EG:10 H<sub>3</sub>PO<sub>4</sub> mixture at 30 V for 1 h which then increased to 6.8 μm and 196.8 nm, respectively by adding 1% of water. The PL result revealed that the number of crystal defects was reduced after the addition of water, which thus improved the separation rate of photo-generated charges. The band gap energy of TNA was reduced from 3.1 to 2.4 eV. It is indicated that the TNA with C and P doping showed improved visible light response. The scavenger test revealed that superoxide and hydroxyl radical are the dominant ROS that contributed to the excellent photo-degradation of MB.

**KEYWORDS** | Carbon and phosphorus co-doped; Catalytic activity; Reactive oxygen species; TiO<sub>2</sub> nanotube arrays

**ABBREVIATIONS** | BQ, benzoquinone; CAN, acetonitrile; CB, conduction band; EDX, energy dispersive X-ray; EG, ethylene glycol; FESEM, field emission scanning electron microscope; MB, methylene blue; Me-OH, methanol; NBE, near band edge; PL, photoluminescence; ROS, reactive oxygen species; TNA, TiO<sub>2</sub> nanotube arrays; VB, valence band; XRD, X-ray diffraction

### CONTENTS

1. Introduction
2. Experimental Procedure

- 2.1. Materials
- 2.2. Anodization
- 2.3. Characterization
- 3. Results and Discussion
  - 3.1. Characteristics of the Prepared Electrolyte
  - 3.2. Current Density Profile of the Anodized Sample
  - 3.3. Morphology of Annealed TNA
  - 3.4. Elemental Analysis
  - 3.5. Crystal Structure Analysis of the Annealed TNA
  - 3.6. Effect of Water Addition on the Morphology of the Nanotubes
  - 3.7. Effect of Water Addition on the Crystal Structure of the Nanotubes
  - 3.8. Photoluminescence (PL)
  - 3.9. Photocatalytic Performance
- 4. Conclusion

## 1. INTRODUCTION

TiO<sub>2</sub> nanotube arrays (TNA) have received considerable attention in numerous applications due to reactive oxygen species (ROS) production that eliminates microbial infections [1, 2], as well as antifouling and self-cleaning [3] properties. TNA with a highly ordered feature generally absorb light with energy greater than the band gap energy, thus exciting electron from the valence band (VB) to the conduction band (CB), while positive holes remain in the VB. These photo-generated electrons and positive holes split the oxygen and water to produce ROS such as hydroxyl radical and superoxide [4, 5]. These ROS attack the toxic organic compounds/microorganisms which are adhered on the TNA surface and destroy them completely through an oxidative mechanism. The self-cleaning and biocidal action of TNA are frequently ascribed to ROS release [6–8]. Unfortunately, TNA can absorb only UV light due to the wide band gap (about 3.2 eV). Therefore, the improvement of ROS production under visible light irradiation has been the goal of numerous investigations. It is considered that cation or anion doping is the effective way to extend the absorption edge of TiO<sub>2</sub> into the visible light region.

Cation doped TiO<sub>2</sub> has been widely studied over the past decades due to its ability to reduce the band gap energy and improve photocatalytic performance under visible light. Lin et al. [9] reported metal ion doping of TiO<sub>2</sub> using alkaline earth metals (Ca<sup>2+</sup>, Sr<sup>2+</sup>, and Ba<sup>2+</sup>), Fe<sup>2+</sup>, Cr<sup>6+</sup>, Co<sup>3+</sup>, Mo<sup>5+</sup>, and rare earth metals (La<sup>3+</sup>, Ce<sup>3+</sup>, Er<sup>3+</sup>, Pr<sup>3+</sup>, Gd<sup>3+</sup>, Nd<sup>3+</sup>, and Sm<sup>3+</sup>)

via different preparation techniques. The majority of cation doping was prepared using co-precipitation, wet impregnation, and sol-gel method [10]. When the metal ions are doped into TiO<sub>2</sub>, an impurity energy level is formed to alter the electron-hole recombination. Transitional metals are either doped or deposited on the TiO<sub>2</sub> surfaces as ionic dopants or metallic nanoparticles. Different methods of doping, and the shift of the absorption edge in the metal ion doped system may have a complex origin, depending on homogeneous substitution of Ti<sup>4+</sup> or segregated metal oxides clusters. Although cation doping can improve the visible spectrum response but the photo-generated electron-hole pair lifetime decreases causing the overall efficiencies to be at a similar level [11]. This is because in cation doping, the doped sites often behave as recombination centers for photo-generated charged carriers due to the substitution of Ti<sup>4+</sup> with metallic ions. Also, transition metal ion doped TiO<sub>2</sub> samples often suffer from thermal instability. These cause the photocatalytic activity of cation-doped TiO<sub>2</sub> to often decrease because of the thermal instability or an increase in carrier recombination centers [12].

Anion doping is another type of elemental doping to modify the band gap of TNA to improve visible response. It has been proven that anion-doped TiO<sub>2</sub>, such as nitrogen, carbon, phosphorus, and sulfur-doped TiO<sub>2</sub>, exhibits visible photo-response and reduces the band gap energy of TiO<sub>2</sub>. This is because of the atomic orbitals of non-metal elements (e.g., N2p, S3p, and C2p) have higher potential energy than O2p [13]. This will form a new valence bands

instead of pure O2p atomic orbital, which reduce the band gap energy without affecting the conduction band level. This doping required the creation of surface oxygen vacancies where the anions will incorporate into the anatase or rutile by substitution in oxygen lattice sites [14]. The anion doped photocatalysts are better for extending the photocatalytic activity of TiO<sub>2</sub> into visible region compared to metal cation doping methods because their impurity states are near the valence band edge and their roles as recombination centers may be minimized. However, the studies regarding the photocatalytic activity of co-doped TiO<sub>2</sub> with two anions are still limited. It is expected that a combination of doping elements could result in an obvious increase in the photocatalytic activity of TiO<sub>2</sub> into the visible light region. In this work, TNA prepared by Ti anodization method in EG containing NH<sub>4</sub>F and various amount of H<sub>3</sub>PO<sub>4</sub> to exhibit different surface properties and catalytic activity due to the generation of diverse diameters, tube lengths, and crystal structures are presented. The effects of C and P doping of the as-prepared TNA arising from electrolyte used for anodization process on catalytic properties via ROS production are investigated and documented.

## 2. EXPERIMENTAL PROCEDURE

### 2.1. Materials

All chemicals used were of analytical grade and purchased from Merck (Kenilworth, NJ, USA). Ti foil (99.6% purity, thickness 0.13 mm, and purchased from Strem Chemical, Newburyport, MA, USA) was used as a substrate to synthesize TNA. The foil was cut into 1 cm × 5 cm in dimension. Ethylene glycol (EG) was used as an electrolyte and carbon source for doping. The solid ammonium fluoride (NH<sub>4</sub>F) was used to prepare the electrolyte to induce fluoride ion to attack the oxide layer on Ti foil and form nanotube structure. Phosphoric acid (H<sub>3</sub>PO<sub>4</sub>) was used as a doping source of P.

### 2.2. Anodization

Anodization was performed in a standard two-electrode system with Ti foil as the working electrode and platinum as the counter electrode. Prior to anodization, the Ti foil was sonicated in ethanol for

15 min, rinsed with deionized water, and then air-dried. After drying, the foil was exposed to an electrolyte consisting different volume ratios of EG and H<sub>3</sub>PO<sub>4</sub> with 0.6% of NH<sub>4</sub>F (Table 1). All the samples were anodized under a constant potential of 30 V and a potential ramp of 1 V/10 sec for 1 h. The anodized samples were then annealed in Ar atmosphere at 400°C for 4 h. The best electrolyte ratio was used to study the effect of water addition on morphology and crystallinity.

### 2.3. Characterization

For the morphology characterization, a field emission scanning electron microscope (FESEM) (SUPRA 35VP ZEISS, Jena, Germany) operating at a working distance of 4 mm with accelerating voltage of 5 kV was used. Cross-sectional measurements were performed on the mechanically bent samples to obtain the thickness of the formed anodic layer. The actual length of the nanotubes was estimated by dividing the length on the micrograph using cos 45°. The chemical stoichiometry of the sample was investigated using energy dispersive X-ray analysis. The crystal phases of the TNA were studied via X-ray diffraction (XRD) using the Bruker D8 (Billerica, MA, USA) at 45 kV and 40 mV. Fluorescence spectra were recorded at room temperature using an LS-55 luminescence spectrometer (Jobin-Yvon HR). The role of ROS from the entire samples was determined by evaluating the photocatalytic activity of the nanocomposite films to degrade methylene blue (MB) aqueous solution. The sample was immersed in 10 ppm of 40 ml of MB and kept in a dark environment for 1 h to attain an equilibrium adsorption state. Then the samples were irradiated under sunlight for a set of irradiation time points. After the degradation, the sample was removed and solution was withdrawn and measured using a UV-Vis spectrophotometer at 644 nm. The photocatalytic experiments were repeated in the presence of radical scavengers to access the participation of different reactive species (hydroxyl radical, superoxide, h<sup>+</sup>) on the photocatalytic reaction. Methanol (Me-OH) [15], acetonitrile (ACN) [16] and benzoquinone (BQ) [17] were selected as scavengers for h<sup>+</sup>, hydroxyl radical, and superoxide, respectively. The experimental conditions are given as follows: MB = 10 ppm, scavenger (Me-OH, ACN, or BQ) concentration = 5 mM and irradiation time = 120 min.

### 3. RESULTS AND DISCUSSION

#### 3.1. Characteristics of the Prepared Electrolyte

The pH of the electrolyte was varied by changing the ratio of  $\text{H}_3\text{PO}_4$ :EG. The results are shown in **Table 1**. The pH of the electrolyte was increased by decreasing the concentration of  $\text{H}_3\text{PO}_4$ . Furthermore, the viscosity of the electrolyte was reduced with  $\text{H}_3\text{PO}_4$  addition.

#### 3.2. Current Density Profile of the Anodized Sample

**Figure 1** shows the current density as a function of anodization time for various electrolyte compositions at constant voltage of 30 V for 1 h. Obviously, the current density profile is influenced by the pH and viscosity of the electrolyte. Samples anodized in electrolyte at high acidic pH (samples P1 and P2) showed different current density profile as compared to other samples (P3 to P5). For sample P1, during the initial step of anodization (first 4 min) an abrupt decrease of current density from  $5.1 \text{ mA/cm}^2$  to  $3.1 \text{ mA/cm}^2$  is observed due to the formation of a barrier layer which induces the voltage drop between Ti (Ti) foil and the electrolyte. This initial process is termed as passivation process as illustrated in the following reaction;  $\text{Ti}^{4+} + 2 \text{H}_2\text{O} \rightarrow \text{TiO}_2 + 4 \text{H}^+$ . In the second stage, the current density is gradually increased to  $4.5 \text{ mA/cm}^2$ . This may be ascribed to a local thinning of the passivated layer by pit formation and random growing pores. This process occurs due to the polarization of Ti-O bond assisted by electric field across the sample [18]. The pits are the pore nucleation center, which will eventually grow into nanotubes with various sizes. The growth of the pits is associated with chemical dissolution ( $\text{TiO}_2 + 4 \text{H}^+ + 6 \text{F}^- \rightarrow \text{TiF}_6^{2-} + 2 \text{H}_2\text{O}$ ).  $\text{TiF}_6^{2-}$  is a water-soluble complex formed by the reaction of fluorine ions and  $\text{Ti}^{4+}$ . This

complex formation aids to prevent Ti-oxide layer formation at the bottom because of the continuous chemical dissolution process. At the third stage (after 50 min), the current density showed a small periodic fluctuation around  $4.6 \text{ mA/cm}^2$  corresponding to quasi-steady state. In this stage, a constant equilibrium is maintained with increasing of anodization time. The fluctuation of current at this stage is probably ascribed to the competition between the growth and dissolution of the oxide layer to form a stable nanotube [19]. The current density profile of P2 is similar to that of P1. However, the observed current density is higher as compared to P1. Moreover, the time taken to reach the quasi-steady state was faster (25 min) as compared to P1 (50 min). This may be associated to the less acidic and more viscous electrolyte condition that moderates the vigorous chemical dissolution process for the pore growth. Sample P3 to P5 have different current density profile as compared to P1 and P2. After an initial exponential decay, the current density is decreased in a monotonic way until it reaches the quasi steady state, without appearing a local minimum. This is ascribed to a different anodization condition which leads to less passivation of the Ti substrate. The growth occurs without previously random pore formation due to less aggressive nature of the EG containing 20% and less  $\text{H}_3\text{PO}_4$  content. The current density of the samples is  $\text{P2} > \text{P1} > \text{P3} > \text{P4} > \text{P5}$ . This finding further supports the absence of local minimum point at current density profile for samples P3 to P5.

#### 3.3. Morphology of Annealed TNA

**Figure 2a–e** shows the FESEM images of Ti anodized samples in different volume ratios of EG and  $\text{H}_3\text{PO}_4$  at 30V for 1 h and subsequently annealed at  $400^\circ\text{C}$  in Ar atmosphere. The different volume ratio of EG and  $\text{H}_3\text{PO}_4$  leads to change in TNA surface morphology. The diameter, length, wall thickness,

**TABLE 1. The pH and volume ratio of the electrolyte**

Sample name	EG	$\text{H}_3\text{PO}_4$	pH
P1	50	50	3.0
P2	60	40	3.5
P3	80	20	4.5
P4	90	10	5.0
P5	100	0	6.6

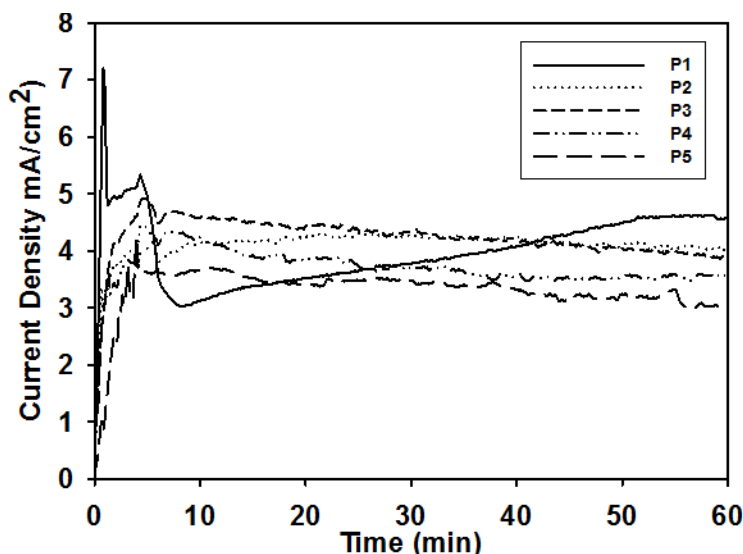


**FIGURE 1.** Current density versus time plot of Ti anodized at 30 V for 1 h in P1, P2, P3, P4, and P5 containing 0.6% of  $\text{NH}_4\text{F}$ .

and aspect ratio of TNA synthesized using different electrolytes are summarized in Table 2. The surface of P1 (Figure 2a) is covered with an oxide layer with irregular features. Some parts are found to be preferentially etched. This could be ascribed to the low pH of the electrolyte leading to the increase in hydrogen ions ( $\text{H}^+$ ). Hence, aggressive chemical dissolution could occur at the top and bottom of nanotubes resulting in an irregular oxide layer. Surface morphology (Figure 2b) shows the formation of ring like structure but the surface is not well ordered. The length of the tubes is very short; approximately 180 nm, indicating that the chemical dissolution is still high and therefore some parts of the nanotubes are preferentially etched to form porous oxide layer. Sample P3 showed the formation of well-ordered TNA (Figure 2c). The length of nanotubes is approximately 1200 nm and the ridges on the circumference of nanotubes are obvious. The ridges at the surface of the nanotubes are caused by high diffusion constant of the electrolyte, which causes a pH burst during the anodization [20]. A similar feature is observed for sample P4 (Figure 2d). However, the length is improved as compared to P3. This is probably attributed to less acidity of the electrolyte, which lowers the chemical dissolution. Furthermore, the results obtained coincide with the current density

plot, which is found to be lower for sample P4 as compared to P3, an affirmation to the lower chemical dissolution of sample P4 for long nanotube formation. For sample P5 (Figure 2e), well ordered nanotubes with a length of 4800 nm is observed. The length of the nanotubes is improved well because pH 6.6 offered a protective environment along the tube wall and pore mouth, which minimized lateral and top dissolution. Other than that, the diameters of the nanotubes are uniform and the walls are smoother. This is ascribed to viscous electrolyte suppressing the pH burst by decreasing the  $\text{H}^+$  formation in the electrolyte.

### 3.4. Elemental Analysis

The chemical stoichiometry of  $\text{TiO}_2$  was investigated using energy dispersive X-ray (EDX) analysis (Table 3). The results indicate that the elements such as Ti, oxygen, phosphorus, and carbon existed in the samples. There are no other impurities observed. The atomic percentage of carbon is in the range of 5.03–8.91% and it is found to be increased with the nanotube length. However, sample P1 is the exceptional case whereby the oxide layer with irregular features seems to have a high carbon content. In contrast, P content is reduced with the length of nanotubes and



**TABLE 2.** Nanotube length, diameter, wall thickness and aspect ratio of Ti anodized in various volume ratio of EG and H<sub>3</sub>PO<sub>4</sub>

Sample	Tube length (μm)	Tube diameter (nm)	Wall thickness (nm)	Aspect ratio
<b>P1</b>	—	—	—	—
<b>P2</b>	0.18	121.8	26.9	1.48
<b>P3</b>	1.2	132.8	26.4	9.04
<b>P4</b>	3.1	103.0	16.1	30.10
<b>P5</b>	4.8	59.0	10.2	81.36

Note: The tube length is after dividing cos 45°.

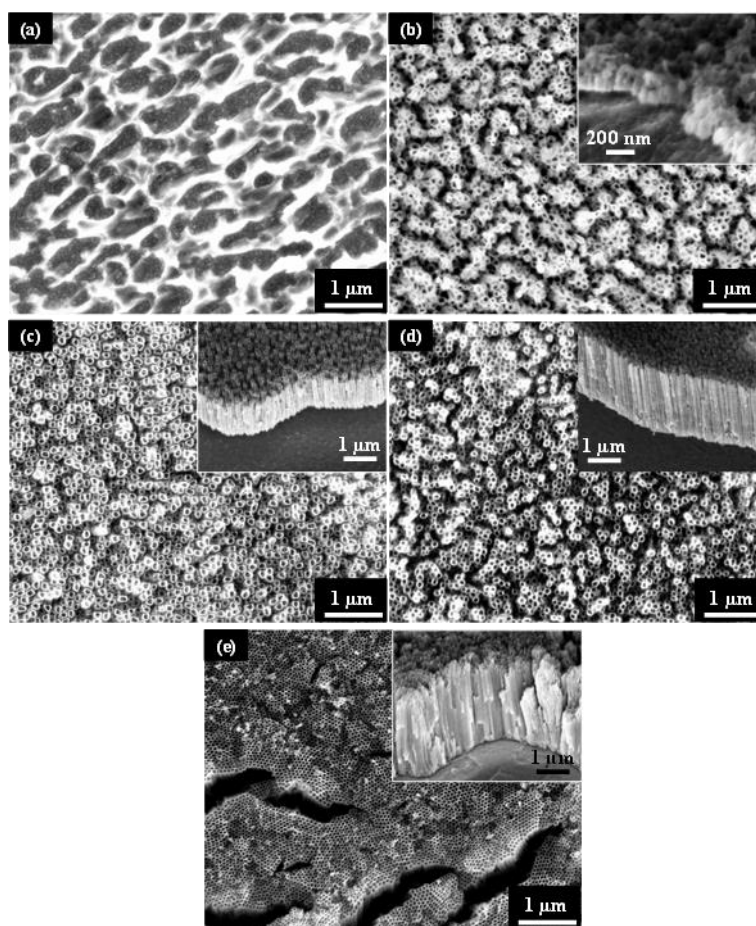


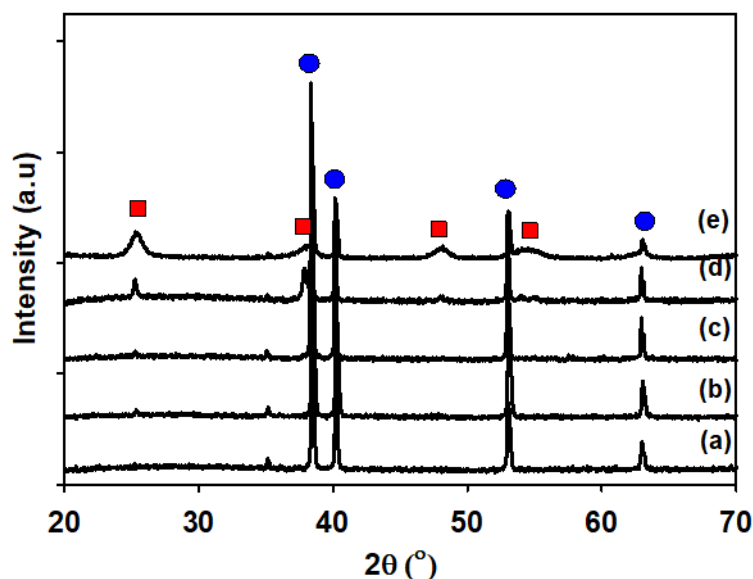
**FIGURE 2.** FESEM image of top view of Ti anodized at 30 V for 1 h in (a) P1, (b) P2, (c) P3, (d) P4, and (e) P5 containing 0.6% of NH<sub>4</sub>F.

this is probably associated with a low content of H<sub>3</sub>PO<sub>4</sub> in the respective electrolytes. It is anticipated that longer nanotubes with a diameter of ~100 nm

that had been co-doped would result in a better photocatalytic activity and therefore electrolyte used for sample P4 was optimized further at higher voltage

**TABLE 3.** Chemical stoichiometry of the TiO<sub>2</sub> investigated using energy dispersive X-ray (EDX) analysis

Sample	Carbon content (%)	Oxygen content (%)	Phosphorus content (%)	Ti content (%)
P1	7.18	23.59	0.46	68.78
P2	5.03	24.06	0.40	70.51
P3	5.53	19.91	0.44	74.12
P4	7.75	56.28	0.18	35.79
P5	8.91	57.78	0.00	33.31

**FIGURE 3.** XRD pattern of Ti anodized at 30 V for 1 h in (a) P1, (b) P2, (c) P3, (d) P4, and (e) P5 containing 0.6% of NH<sub>4</sub>F and subsequent annealed in argon atmosphere at 400°C for 4 h. Blue circle, Ti; red square, anatase.

(60 V) with water addition and discussed in the later section.

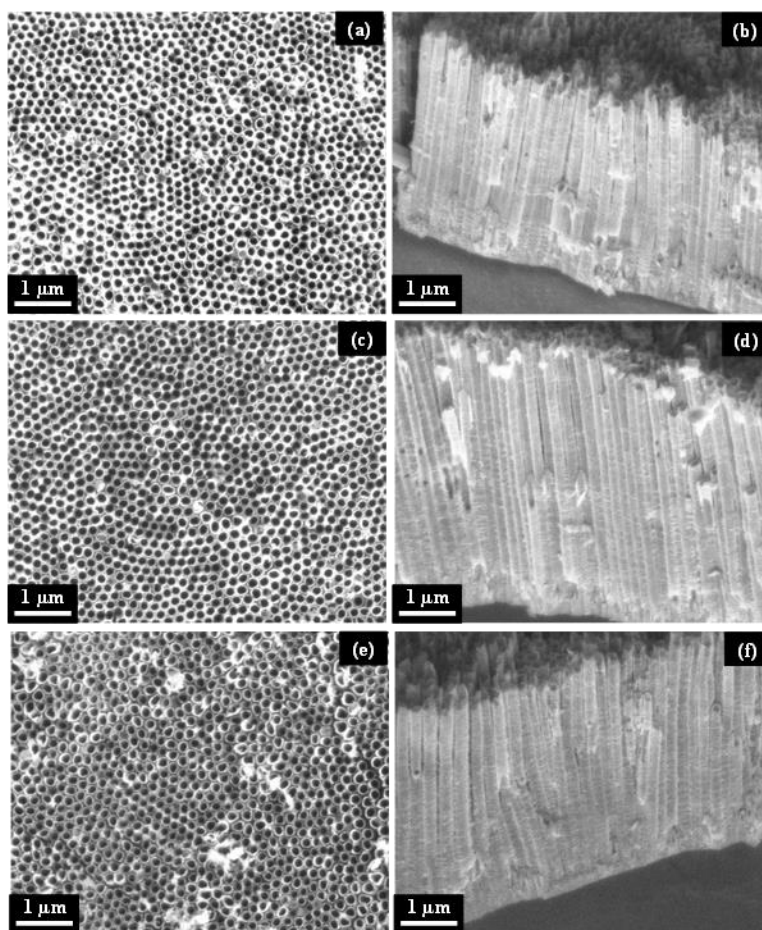
### 3.5. Crystal Structure Analysis of the Annealed TNA

Figure 3 shows the XRD pattern of P1–P5. Only the diffraction from Ti substrate is seen for sample P1. This is caused by the low thickness of the TNA layer. For samples P2 and P3, a small diffraction peak of anatase at 25.2° corresponding to (101) plane is observed. These results reflect that the phase transformation to anatase was achieved at 400°C, but the thickness of TiO<sub>2</sub> is still very small to be clearly

measured using XRD. However, the anatase peak is clearly observed for samples P4 and P5, which have a longer length.

### 3.6. Effect of Water Addition on the Morphology of The Nanotubes

Water (0.5, 1.0, and 2.0%) was added to the electrolytes and the samples were denoted as P4-H05, P4-H10, and P4-H20, respectively. The pH of the electrolyte before and after anodization is approximately 5.0. The variations of surface morphology of TNA with different water volume content are exhibited in Figure 4a–4f, while Figure 2d above refers to the



**FIGURE 4.** The top FESEM image of Ti anodized at 60 V for 1 h in (a) P4-H05, (c) P4-H10, and (e) P4-H20 containing 0.6%  $\text{NH}_4\text{F}$ . The b, d, and f are cross sectional view of the respective sample.

**TABLE 4.** The dimensions of the tubes formed, C and P content of Ti anodized at 60 V for 1 h in various electrolytes and 0.6%  $\text{NH}_4\text{F}$

Sample	Tube length ( $\mu\text{m}$ )	Tube diameter (nm)	Wall thickness (nm)	Aspect ratio	C content (%)	P content (%)
P4	5.1	177.7	17.0	28.7	10.92	0.40
P4-H05	4.3	183.5	29.9	23.4	4.96	0.59
P4-H10	6.8	196.8	27.5	34.6	5.02	0.34
P4-H20	5.4	194.4	36.3	27.8	4.76	0.49

sample without water addition. The dimensions such as tube length, tube diameter, wall thickness, aspect

ratio, carbon, and phosphorus content of TNA are summarized in **Table 4**.



Based on the FESEM images, the tube length is significantly affected by water addition as compared to the tube diameter. When 0.5% of water is added, there is no significant change in tube length. The tube length was 4.3  $\mu\text{m}$  and increased to 6.8  $\mu\text{m}$  for 1.0% of water. This is attributed to hydroxyl ion availability in  $\text{H}_2\text{O}$  for oxide formation [21]. It is suggested that water addition causes hydroxyl ion injection from the electrolyte into the oxide film during anodization. It means that hydroxyl ions will be injected into the body of the oxide layer and affect the structure by impeding the ion transport through the barrier layer. This is important to move the metal-oxide interface further into the metal [18]. Also, adding water to the electrolyte will facilitate  $\text{NH}_4\text{F}$  dissolution and ensure field-assisted etching of the Ti foil at the pore bottom [18]. Nevertheless, when the water content exceeds certain limit, the tubes become much shorter. This is clearly seen for the Ti anodized in 2.0%  $\text{H}_2\text{O}$  that has tubes with 5.4  $\mu\text{m}$ . According to Valota et al. [22], excess oxygen evolution with

fore, it is important to find an optimum water content, which favors the formation of long nanotubes. As for the present work, a 90:10 (EG to  $\text{H}_3\text{PO}_4$ ) ratio with 1% of water is the best electrolyte for the formation of long TNA.

### 3.7. Effect of Water Addition on the Crystal Structure of The Nanotubes

**Figure 5** shows the XRD pattern of the annealed TNA formed in the electrolyte containing various amount of water. The crystalline phases are similar to those of sample P4. However, the intensity of anatase peak is prominent as the volume of water is high. This is ascribed to the formation of a thick oxide layer and improved anatase crystallinity.

### 3.8. Photoluminescence (PL)

**Figure 6** shows the room temperature PL spectra of P4, P4-H05, P4-H10, and P4-H20. Two PL emission

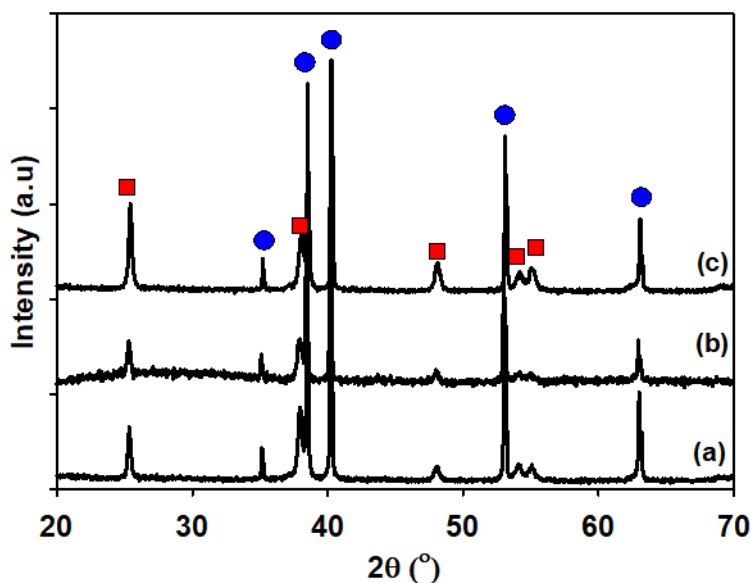


**FIGURE 5.** XRD pattern of Ti anodized at 30 V for 1 h in (a) P4-H05, (b) P4-H10, and (c) P4-H20 containing 0.6% of  $\text{NH}_4\text{F}$  and subsequent annealed in argon atmosphere at 400°C for 4 h. Blue circle, Ti; red square, anatase.

high water addition reduces the charge available for film growth, resulting in shorter nanotubes. There-

peaks are identified: a sharp UV emission at 400 nm and a broad visible light emission at 500 nm. The

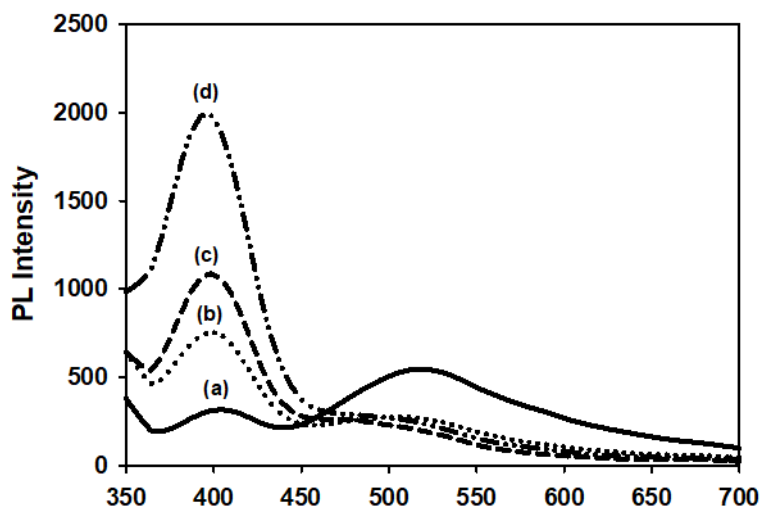


**FIGURE 6.** PL spectra of Ti anodized at 30 V for 1 h in (a) P4, (b) P4-H05, (c) P4-H10, and (d) P4-H<sub>2</sub>O containing 0.6% of NH<sub>4</sub>F and subsequent annealed in argon atmosphere at 400°C for 4 h.

UV emission is assigned to near band edge (NBE) emission by recombination of free excitons while visible emission is related to crystal defects ascribed to O vacancies. The  $I_{uv}/I_{vis}$  ratio of TNA anodized without water (P4) was 0.57 and that for P4-H05, P4-H10, and P4-H20 were 2.73, 4.66, and 8.32, respectively. The high ratio of  $I_{uv}/I_{vis}$  for samples with water addition reveals good crystal quality as compared to samples without water (P4). This result suggests that the number of defects acting as recombination centers in TNA was reduced and the separation rate of photogenerated charges was significantly increased with water addition, thus improving the ROS release. Besides, the outcomes affirm that the water addition causes hydroxyl ion injection from the electrolyte into the oxide film during anodization, thus minimizing the presence of oxygen vacancies.

### 3.9. Photocatalytic Performance

Photodegradation of MB was conducted to test the photocatalytic activity of the TNA (P3, P4, P5, P4-H10). The kinetics of all photocatalytic reactions using TNA (P3, P4, P5, P4-H10) can be expressed by the Langmuir–Hinshelwood model in the equation,  $\ln(C/C_0) = kt$ , which represents the pseudo first-order reaction and where  $k$  is the apparent rate constant of reaction under the given experimental conditions and

$t$  is time. Variations of the relative concentrations ( $C/C_0$ ) (where  $C$  is concentration, which varies with time, and  $C_0$  is the equilibrium concentration) of MB with time. **Figure 7** shows the photodegradation of MB under sunlight and **Table 5** summarizes the initial first-order degradation rate constants for photodegradation of MB.

As shown in **Figure 7**, after 120 min of sunlight irradiation, the photocatalytic activity of TNA is in an order of P4-H10 > P4 > P3 > P5. The higher degradation efficiency of P4-H10 may be partially attributed to the synergistic effect of C and P doping and its higher aspect ratio of 34.6 for P4-H10 versus 28.7 for P4, and 9.04 for P3. Although P5 has the highest aspect ratio (81.36), the fact that it does not dope with P has reduced its photocatalytic performance. The high aspect ratio and effective charge separation due to doping are conducive to increased efficiency due to the higher availability of active sites for ROS generation and greater opportunity for the interaction between photo-generated electrons/holes or ROS and contaminants on the surface of the photocatalyst.

The first-order photo-degradation rates of entire samples were shown in **Table 5**.  $k$  [P4-H10 + MB] shows to be greater than that obtained with [P4 + MB], [P3 + MB], and [P5 + MB] with a calculated  $k$  of 5.01, 2.07, 1.32, and  $1.20 \times 10^{-2} \text{ min}^{-1}$ , respective-

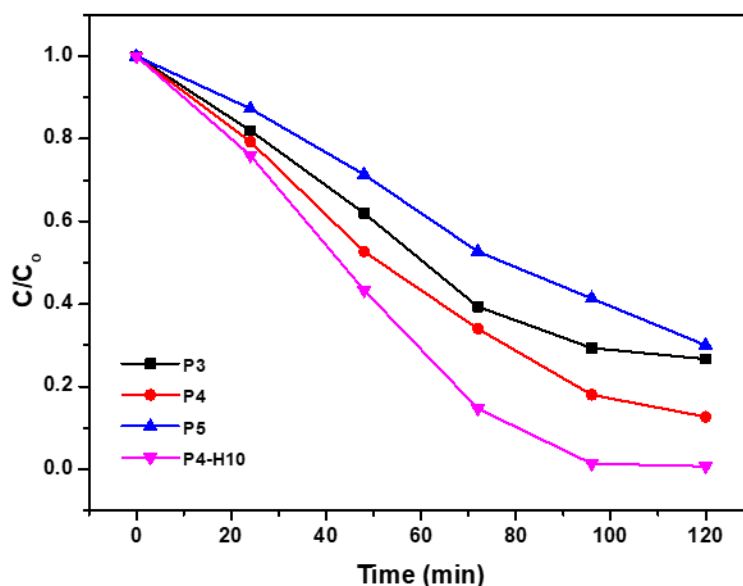


**FIGURE 7.** Relative concentration versus irradiation time during the photocatalytic experiments using TNA (P3, P4, P5, and P4-H10) as the photocatalyst for MB photodegradation under sunlight.

ly. It can be seen that the  $k$  values of P4 + MB and P4-H10 + MB are declined in the presence of ROS scavengers. To further understand the role of photo-generated ROS, photodegradation of MB by TNA (P4 and P4-H10) was characterized in the presence of two different ROS scavengers at 5 mM: *n*-benzoquinone (BQ which acts as a superoxide scavenger) and acetonitrile (ACN, a preferential hydroxyl radical scavenger). Addition of BQ, which helps discern the role of superoxide (Figure 8), had a greater

impact on the degradation of MB by P4-H10 (photodegradation reduction by 90%) than by P4 (13% reduction). This suggests that superoxide-mediated degradation plays a more significant role in the presence of P4-H10 compared to P4. Meanwhile, the degradation of MB in the presence of ACN was more pronounced with P4 compared to P4-H10 with rate of reduction by 45% and 35%, respectively (Table 5). This result confirms the critical role of hydroxyl radical in MB degradation by P4.

**TABLE 5.** First order photodegradation rates

Material/conditions	1 <sup>st</sup> order degradation rate (min <sup>-1</sup> ± standard deviation)
P3 + MB	1.32 ± 0.4
P4 + MB	2.07 ± 0.8
P5 + MB	1.20 ± 0.5
P4-H10 + MB	5.01 ± 0.5
P4 + MB + BQ	1.80 ± 1.5
P4 + MB + ACN	0.73 ± 0.8
P4 + MB + Me-OH	1.90 ± 0.3
P4-H10 + MB + BQ	2.50 ± 0.4
P4-H10 + MB + ACN	3.25 ± 0.8
P4-H10 + MB + Me-OH	4.51 ± 0.5

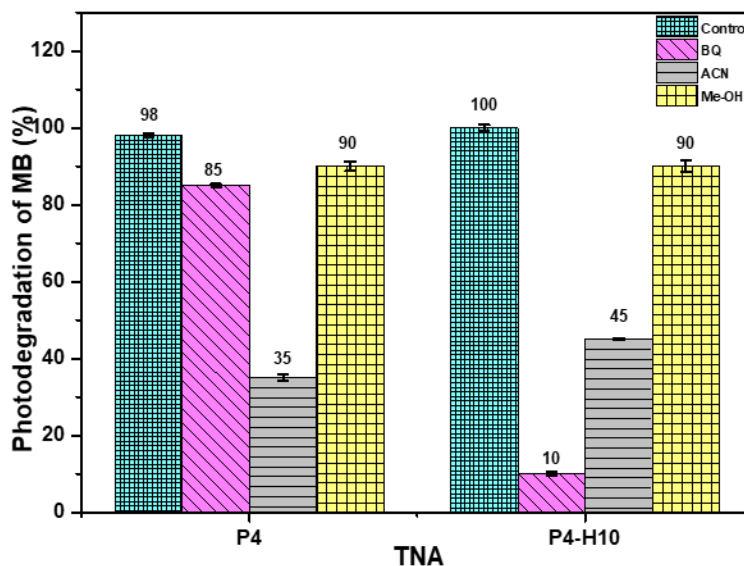


**FIGURE 8.** Relative concentration versus irradiation time during the photocatalytic experiments using TNA (P3, P4, P5, and P4-H10) as the photocatalyst for MB photodegradation under sunlight.

Furthermore, it is clearly seen that the addition of Me-OH induced a small change in the photodegradation of MB (Figure 8), suggest that superoxide and hydroxyl radical are the main reactive species involved in the photodegradation of MB when compared to  $h^+$  for both photocatalysts.

The possible reaction mechanism of co-doped TNA photocatalyst under light irradiation is shown in Figure 9. When the photocatalyst is illuminated by light with photons energy higher than the band gap of  $TiO_2$ , electrons ( $e^-$ ) in the VB can be excited to the CB, resulting in generation of the same amount of holes ( $h^+$ ). For pure TNA, these photo-generated electrons and holes readily recombine within nanoseconds. However, due to the presence of C and P trap center, the recombination of photo-generated electron-hole charge carriers is markedly reduced. As reported in our previous work [21], the adsorbed carbon is identified to narrow the band gap energy by the mixing of C2p and O2p states [23], therefore acting as a  $h^+$  trap to reduce the recombination of photo-generated charge carriers. Besides, the photo-generated  $e^-$  is excited from interstitial carbon via photon ( $h\nu$ ) excitation and subsequently ejected into the  $Ti3d$  state of  $TiO_2$  [24–26], and then transferred to CB of P that positioned below the  $Ti3d$

state. The electrons in this state can further react with  $O_2$  absorbed on the surface of the photocatalyst to generate superoxide. At the same time,  $h^+$  in the VB of  $TiO_2$  transfer to C trap center thus combine with  $H_2O$  to produce active hydroxyl radicals. The existence of P and C not only reduces the recombination of the photoinduced electrons and holes, but also prolongs the life time of the photogenerated pairs. Therefore, these reactive radical species of superoxide, hydroxyl radical,  $h^+$ , and  $e^-$  are highly reactive and capable of degrading MO into  $H_2O$  and  $CO_2$ . Moreover, according to Zheng et al. [27], doped phosphorous existed in a pentavalent oxidation state replacing the  $Ti^{4+}$  in anatase lattice in the form of Ti-O-P bonds. P species in the  $TiO_2$  lattice is the dominant group responsive to visible light.

#### 4. CONCLUSION

In conclusion, C and P co-doped TNA was successfully fabricated via anodization using the EG and  $H_3PO_4$  electrolyte mixture with 0.66% of  $NH_4F$ . The presence of C and P in TNA P4-H10 induces the formation of a new energy state above VB, which is attributed to the C2p state of the interstitial carbon

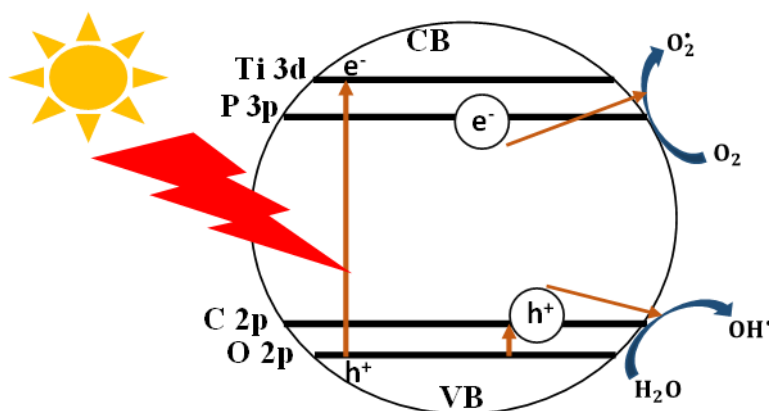


**FIGURE 9. A possible mechanism of MB degradation by C and P doped TNA under sunlight.**  $O_2^{\cdot -}$ , superoxide;  $OH^{\cdot}$ , hydroxyl radical.

and new energy state below the CB, corresponding to Ti-O-P state. Therefore, P and C doping improves the light absorption and photodegradation as compared to P5 (42%). This study also reveals that various ROS including superoxide and hydroxyl radicals are the dominant species generated when the TNA was irradiated by sunlight. The research results also demonstrate that the quantities of the generated ROS increase when C and P were co-doped in TNA.

## ACKNOWLEDGMENTS

The authors are thankful to the Ministry of Education (MOE) Malaysia for funding this work under Transdisciplinary Research Grant Scheme (TRGS) grant no. 6769002. The authors are very grateful to Universiti Sains Malaysia (USM) for providing the necessary facilities to carry out the research work and financial support under Research University (RU) grant no. 814281. The authors declare no conflicts of interest.

## REFERENCES

1. Durairaj B, Xavier T, Muthu S. Fungal generated titanium dioxide nanoparticles for UV Protective and bacterial resistant fabrication. *Int J Eng Sci Technol* 2014; 6(9):621.
2. Maness P-C, Smolinski S, Blake DM, Huang Z, Wolfrum EJ, Jacoby WA. Bactericidal activity of photocatalytic  $TiO_2$  reaction: toward an understanding of its killing mechanism. *Appl Environ Microbiol* 1999; 65(9):4094–8.
3. Chen C-C, Lin J-S, Diau EW-G, Liu T-F. Self-cleaning characteristics on a thin-film surface with nanotube arrays of anodic titanium oxide. *Appl Phys A* 2008; 92(3):615–20. doi: 10.1007/s00339-008-4546-7.
4. Wang J, Guo Y, Liu B, Jin X, Liu L, Xu R, et al. Detection and analysis of reactive oxygen species (ROS) generated by nano-sized  $TiO_2$  powder under ultrasonic irradiation and application in sonocatalytic degradation of organic dyes. *Ultrason Sonochem* 2011; 18(1):177–83.
5. Guo X, Li Q, Zhang M, Long M, Kong L, Zhou Q, et al. Enhanced photocatalytic performance of *N*-nitrosodimethylamine on  $TiO_2$  nanotube based on the role of singlet oxygen. *Chemosphere* 2015; 120:521–6.
6. Wu D, Long M, Zhou J, Cai W, Zhu X, Chen C, et al. Synthesis and characterization of self-cleaning cotton fabrics modified by  $TiO_2$  through a facile approach. *Surf Coat Technol* 2009; 203(24):3728–33.
7. Chan CMN, Ng AMC, Fung MK, Cheng HS, Guo MY, Djurišić AB, et al. Antibacterial and photocatalytic activities of  $TiO_2$  nanotubes. *J Exp Nanosci* 2013; 8(6):859–67.
8. Luan X, Wang Y. Preparation and photocatalytic



- activity of Ag/bamboo-type TiO<sub>2</sub> nanotube composite electrodes for methylene blue degradation. *Mater Sci Semicond Process* 2014; 25:43–51.
9. Lin D, Cao G-X, Ying M, Jia X-L, Ye G-T, Guan S-K. Enhanced photocatalytic degradation properties of nitrogen-doped titania nanotube arrays. *Trans Nonferrous Met Soc China* 2009; 19(6):1583–7.
  10. Shon H, Phuntsho S, Okour Y, Cho D-L, KK S, Li J, et al. Visible light responsive titanium dioxide (TiO<sub>2</sub>). *J Korean Indust Eng Chem* 2008.
  11. Varma RS, Thorat N, Fernandes R, Kothari D, Patel N, Miotello A. Dependence of photocatalysis on charge carrier separation in Ag-doped and decorated TiO<sub>2</sub> nanocomposites. *Catal Sci Technol* 2016; 6(24):8428–40.
  12. Wong M-S, Hsu S-W, Rao KK, Kumar CP. Influence of crystallinity and carbon content on visible light photocatalysis of carbon doped titania thin films. *J Mol Catal A: Chem* 2008; 279(1):20–6. doi: 10.1016/j.molcata.2007.09.024.
  13. Tang X, Li D. Sulfur-doped highly ordered TiO<sub>2</sub> nanotubular arrays with visible light response. *J Phys Chem C* 2008; 112(14):5405–9.
  14. Zhang Y, Fu W, Yang H, Liu S, Sun P, Yuan M, et al. Synthesis and characterization of P-doped TiO<sub>2</sub> nanotubes. *Thin Solid Films* 2009; 518(1):99–103. doi: 10.1016/j.tsf.2009.06.051.
  15. Cavicchioli A, Gutz IG. Effect of scavengers on the photocatalytic digestion of organic matter in water samples assisted by TiO<sub>2</sub> in suspension for the voltammetric determination of heavy metals. *J Braz Chem Soc* 2002; 13(4):441–8.
  16. Trandafilović L, Jovanović D, Zhang X, Ptasińska S, Dramićanin M. Enhanced photocatalytic degradation of methylene blue and methyl orange by ZnO:Eu nanoparticles. *Appl Catal B: Environ* 2017; 203:740–52.
  17. Pelaez M, Falaras P, Likodimos V, O'Shea K, Armah A, Dunlop PS, et al. Use of selected scavengers for the determination of NF-TiO<sub>2</sub> reactive oxygen species during the degradation of microcystin-LR under visible light irradiation. *J Mol Catal A: Chem* 2016; 425:183–9.
  18. Grimes CA, Mor GK. *TiO<sub>2</sub> Nanotube Arrays: Synthesis, Properties, and Applications*. Springer, Berlin, Germany. 2009.
  19. Sreekantan S, Lockman Z, Hazan R, Tasbihi M, Tong LK, Mohamed AR. Influence of electrolyte pH on TiO<sub>2</sub> nanotube formation by Ti anodization. *J Alloys Compd* 2009; 485(1):478–83.
  20. Macak JM, Tsuchiya H, Schmuki P. High-aspect-ratio TiO<sub>2</sub> nanotubes by anodization of titanium. *Angew Chem Int Ed Engl* 2005; 44(14):2100–2. doi: 10.1002/anie.200462459.
  21. Sreekantan S, Saharudin KA, Lockman Z, Tzu TW. Fast-rate formation of TiO<sub>2</sub> nanotube arrays in an organic bath and their applications in photocatalysis. *Nanotechnol* 2010; 21(36):365603. doi: 10.1088/0957-4484/21/36/365603.
  22. Valota A, LeClere D, Skeldon P, Curioni M, Hashimoto T, Berger S, et al. Influence of water content on nanotubular anodic titania formed in fluoride/glycerol electrolytes. *Electrochimica Acta* 2009; 54(18):4321–7.
  23. Krengvirat W, Sreekantan S, Mohd Noor AF, Negishi N, Yul Oh S, Kawamura G, et al. Carbon-incorporated TiO<sub>2</sub> photoelectrodes prepared via rapid-anodic oxidation for efficient visible-light hydrogen generation. *Int J Hydrogen Energy* 2012; 37(13):10046–56. doi: 10.1016/j.ijhydene.2012.04.004.
  24. Park JH, Kim S, Bard AJ. Novel carbon-doped TiO<sub>2</sub> nanotube arrays with high aspect ratios for efficient solar water splitting. *Nano Lett* 2006; 6(1):24–8. doi: 10.1021/nl051807y.
  25. Chen D, Jiang Z, Geng J, Wang Q, Yang D. Carbon and nitrogen co-doped TiO<sub>2</sub> with enhanced visible-light photocatalytic activity. *Indust Eng Chem Res* 2007; 46(9):2741–6.
  26. Kuznetsov VN, Serpone N. On the origin of the spectral bands in the visible absorption spectra of visible-light-active TiO<sub>2</sub> specimens analysis and assignments. *J Phys Chem C* 2009; 113(34):15110–23.
  27. Zheng R, Lin L, Xie J, Zhu Y, Xie Y. State of doped phosphorus and its influence on the physicochemical and photocatalytic properties of P-doped titania. *J Phys Chem C* 2008; 112(39):15502–9.